

Excellent magnetic softness-magnetization synergy and suppressed defect activation in soft magnetic amorphous alloys by magnetic field annealing

Qiang Luo^{a,1}, Donghui Li^{a,1}, Mingjuan Cai^{a,1}, Siyi Di^a, Zhengguo Zhang^a, Qiaoshi Zeng^b, Qianqian Wang^a, Baolong Shen^{a,*}

^a School of Materials Science and Engineering, Jiangsu Key Laboratory of Advanced Metallic Materials, Southeast University, Nanjing 211189, China

^b Center for High Pressure Science and Technology Advanced Research, Shanghai 201203, China



ARTICLE INFO

Article history:

Received 14 September 2021

Revised 2 November 2021

Accepted 4 November 2021

Available online 29 January 2022

Keywords:

Fe-based amorphous alloy

Soft magnetic performance

Magnetic field annealing

Heterogeneous structure

Defect activation

ABSTRACT

Fe-based amorphous alloys with high saturation magnetic flux density (B_s) are increasingly attractive from both scientific and technological points of view, however, they usually suffer from the trade-off between magnetization and softness. In this work, we explore the soft magnetic properties (SMPs), magnetic and atomic structures, and defect activation during creep deformation of as-quenched and annealed $\text{Fe}_{82.65-x}\text{Co}_x\text{Si}_2\text{B}_{14}\text{Cu}_{1.35}$ ($x = 0\text{--}20$) amorphous alloys (AAs). Improved magnetic softness-magnetization synergy has been realized in all these alloys by field annealing. Particularly, superb SMPs with superhigh B_s of 1.86 T, low coercivity of 1.2 A/m and high effective permeability of 16300 are obtained in the $\text{Fe}_{66.65}\text{Co}_{16}\text{Si}_2\text{B}_{14}\text{Cu}_{1.35}$ AA. The locally regularized arrangement of domains, homogenized structure with less structural/magnetic defects and suppressed crystal-like ordering by field annealing contribute synergistically to the superb SMPs. Besides, the relaxation time spectra obtained from creep deformation indicate less liquid-like and solid-like defects activated in the field-annealed AA, which is correlated with the structural homogenization and superb SMPs. This work provides new and comprehensive insight into the interplay among external field, heterogeneous structure, SMPs and defect activation of Fe-based AAs, and offers a promising pathway for softening amorphous alloys with high B_s .

© 2022 Published by Elsevier Ltd on behalf of The editorial office of Journal of Materials Science & Technology.

1. Introduction

Soft magnetic materials play a crucial role in realizing high efficiency in electrical and electronic devices. Thereinto, Fe-based amorphous alloys (AAs) have attracted worldwide interests due to their excellent magnetic properties such as high saturation magnetic flux density (B_s), high effective permeability (μ_e), low coercivity (H_c) and low core loss [1–3]. Besides, these alloys exhibit other advantages of good mechanical properties, low annealing temperature and simple annealing process [4,5]. Nevertheless, the relatively lower B_s (<1.7 T typically) of AAs than that of Si-steel (~2.0 T) limits their broader commercial applications [6]. To meet the accelerating requirement of miniaturization of devices and high efficiency, great efforts have been made to enhance B_s of AAs by increasing Fe content [7], partial replacement of Fe with

Co [8], optimizing metalloid elements [9], and nanocrystallization through annealing [10]. Usually, a higher Fe content is conducive to larger B_s , but the Fe content of ~85 at.% approaches the upper limit for amorphous formation [2]. Besides, it is found that Co-doping can enhance B_s more effectively than other composition design strategies without deteriorating the amorphous forming ability and manufacturability in some low FeCo content AAs [11,12]. However, further increasing the FeCo content to obtain high B_s will deteriorate magnetic softness. And this dilemma cannot be solved by normal annealing treatment, which usually causes only slightly improved or even worse soft magnetic performances [13,14]. It has been documented that magnetic field annealing (FA) can enhance the soft magnetic properties (SMPs) of some Fe-based AA and nanocrystalline systems by modulating domain structure and inducing a uniaxial anisotropy [15–18]. However, the B_s in most reported AAs is still below 1.77 T and the underlying structural mechanism is elusive [19,20]. Nanocrystallization of high B_s AAs by annealing encounters relatively poor manufacturability and non-uniformity [21]. Thus, developing high B_s Fe-based AAs with low H_c by combining composition design with effective processing

* Corresponding author.

E-mail address: bishen@seu.edu.cn (B. Shen).

¹ These authors contributed equally to this work.

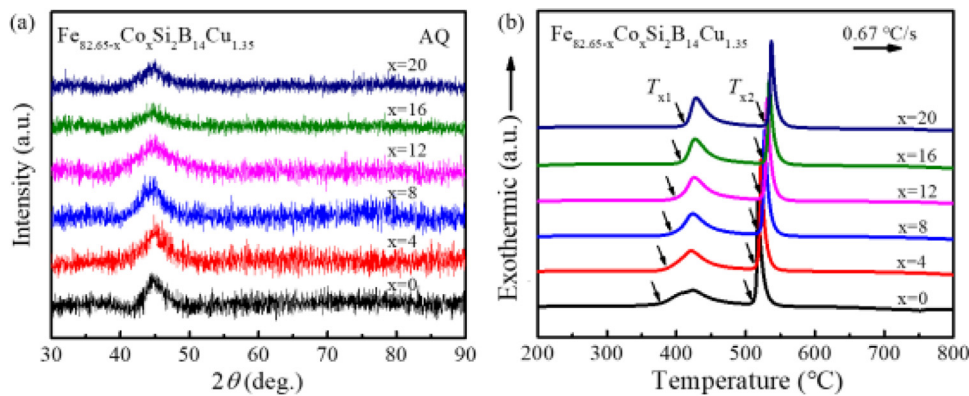


Fig. 1. (a) XRD patterns and (b) DSC curves of the as-quenched $\text{Fe}_{82.65-x}\text{Co}_x\text{Si}_2\text{B}_{14}\text{Cu}_{1.35}$ ($x = 0\text{--}20$) ribbons.

technique requires to be solved urgently, but which suffers from a long-standing challenge of the magnetic softness-magnetization trade-off.

In this work, the $\text{Fe}_{82.65-x}\text{Co}_x\text{Si}_2\text{B}_{14}\text{Cu}_{1.35}$ ($x = 0, 4, 8, 12, 16, 20$) AAs were designed by partially substituting Co for Fe based on Fe-Si-B-Cu, to increase B_s and thermal stability in their amorphous states. The base alloy $\text{Fe}_{82.65}\text{Si}_2\text{B}_{14}\text{Cu}_{1.35}$ has good SMPs in its nanocrystalline state, but systematical investigation of SMPs in its amorphous state is lacking [22]. The P and C elements are not considered since they are unfavorable in mass production. And the Cu content keeps unchanged in this Co-adopting series of AAs to produce additional heterogeneity arising from the positive enthalpy of mixing between Cu and Fe (Co). The enhanced structural heterogeneity facilitates investigation of the FA-heterogeneity-SMP relationship and promotes the local aggregation of elements (opening space to further improve SMPs by FA). The influence of FA on SMPs, magnetic domain structure, and heterogeneous atomic structure, defect activation during creep deformation was systematically investigated. In contrast with the slight improvement or even deterioration of magnetic softness after normal annealing (NA), significant improvement of SMPs is observed after FA, especially for the alloys with compositions of $x \geq 8$. In particular, super-high B_s of 1.86 T and low H_c of 1.2 A/m were achieved in $\text{Fe}_{66.65}\text{Co}_{16}\text{Si}_2\text{B}_{14}\text{Cu}_{1.35}$ alloy after FA at 370 °C under an external magnetic field of 0.1 T, showing excellent magnetic softness-magnetization synergy. The combined effects of causing a uniaxial anisotropy along the direction of applied field, forming uniform strip domains with large width and smooth edge, homogenizing the local structure and suppressing the structure ordering by FA contribute to the superb SMPs. In addition, from the relaxation time spectra obtained from nanoindentation creep deformation experiment, it is found that FA can further suppress the activation of liquid-like and solid-like defects with distinct magnetic exchange interactions from their surroundings, which is related with the enhanced SMPs.

2. Experimental methods

Alloy ingots with nominal compositions of $\text{Fe}_{82.65-x}\text{Co}_x\text{Si}_2\text{B}_{14}\text{Cu}_{1.35}$ alloys ($x = 0, 4, 8, 12, 16, 20$) were prepared by induction melting the mixtures of high purity elements of Fe (99.99%), Co (99.9%), Si (99.99%), B (99.5%) and Cu (99.99%) under an argon atmosphere. Amorphous ribbons with a width of about 1.2 mm and a thickness of 20–25 μm were fabricated by single-roller melt spinning under an argon atmosphere. Samples with a length of 60 mm were isothermally annealed at different temperatures between 270–410 °C for 15 min (or 5 min). The annealing process includes the following steps: (1) sealing the ribbon sample in a quartz tube under a vacuum atmosphere (5×10^{-3} Pa), (2) putting the tube into the furnace

chamber already at a required annealing temperature and holding for 15 min or 5 min, (3) pulling out the tube and quenching it in water to room temperature. The NA was carried out without an applied magnetic field and FA with an applied field of 0.1 T along the ribbon (denoted as “longitudinal magnetic field”). The microstructure of samples was examined by X-ray diffraction (XRD, Bruker D8 Discover) with $\text{CuK}\alpha$ radiation, synchrotron XRD, and transmission electron microscopy (TEM, Talos F200X) equipped with energy-dispersive X-ray spectroscopy (EDS). Synchrotron radiation XRD was conducted on the NA and FA ribbons of $\text{Fe}_{66.65}\text{Co}_{16}\text{Si}_2\text{B}_{14}\text{Cu}_{1.35}$ alloy at Sector 15U1 of the Shanghai Synchrotron Radiation Facility (SSRF). The photon energy was 20 keV corresponding to an X-ray wavelength of 0.6199 Å, and the beam size was $3 \times 3 \mu\text{m}^2$. For high angle annular dark-field (HAADF) imaging, a probe semi-convergence angle of 10.5 mrad and collection semi-angle of 58–200 mrad were used. Thermal analysis was carried out on differential scanning calorimeter (DSC, NETZSCH 404 F3). The Curie temperature (T_C) was measured by SQUID magnetometer (MPMS, Quantum Design) in a field of 0.02 T with a heating rate of 0.16 °C /s. H_c and μ_e were obtained by a dc B - H loop tracer (RIKEN BHS-40) under a maximum applied magnetic field of 1 kA/m and an impedance analyzer (E4990A) under a field of 1 A/m. B_s was measured by a vibrating sample magnetometer (VSM, Lake Shore 7410) under a magnetic field up to 800 kA/m at room temperature. Magnetic force microscopy (MFM) was conducted to record the local domain structure with an Asylum Research MFP-3D AFM. The magnetic tip was kept a lift height of 100 nm. The nanoindentation test was performed on a NanoTest Vantage (Micro Materials Ltd) with a standard Berkovich diamond indenter. Tests at constant loading rates of 0.5, 10, and 50 mN/s were conducted to the prescribed load limit of 80 mN followed by a holding period of 120 s to monitor the creep displacement and then unloaded at the same loading rates. Five independent measurements were carried out under each condition.

3. Results and discussion

3.1. Soft magnetic performance

All the as-quenched (AQ) ribbons with different Co contents show the amorphous structure as indicated from the XRD patterns of Fig. 1(a) without detectable shift of diffraction hump. The DSC curves in Fig. 1(b) of all the AQ ribbons demonstrate a two-stage of the crystallization process, with the first exothermic peak corresponding to the formation of α -(Fe, Co) phase and the second one to Fe-B compounds [23]. When increasing the Co content from $x=0$ to 20, the primary crystallization temperature (T_{x1}) and the second one (T_{x2}) increase from 379 and 509 °C to 411 and 534 °C,

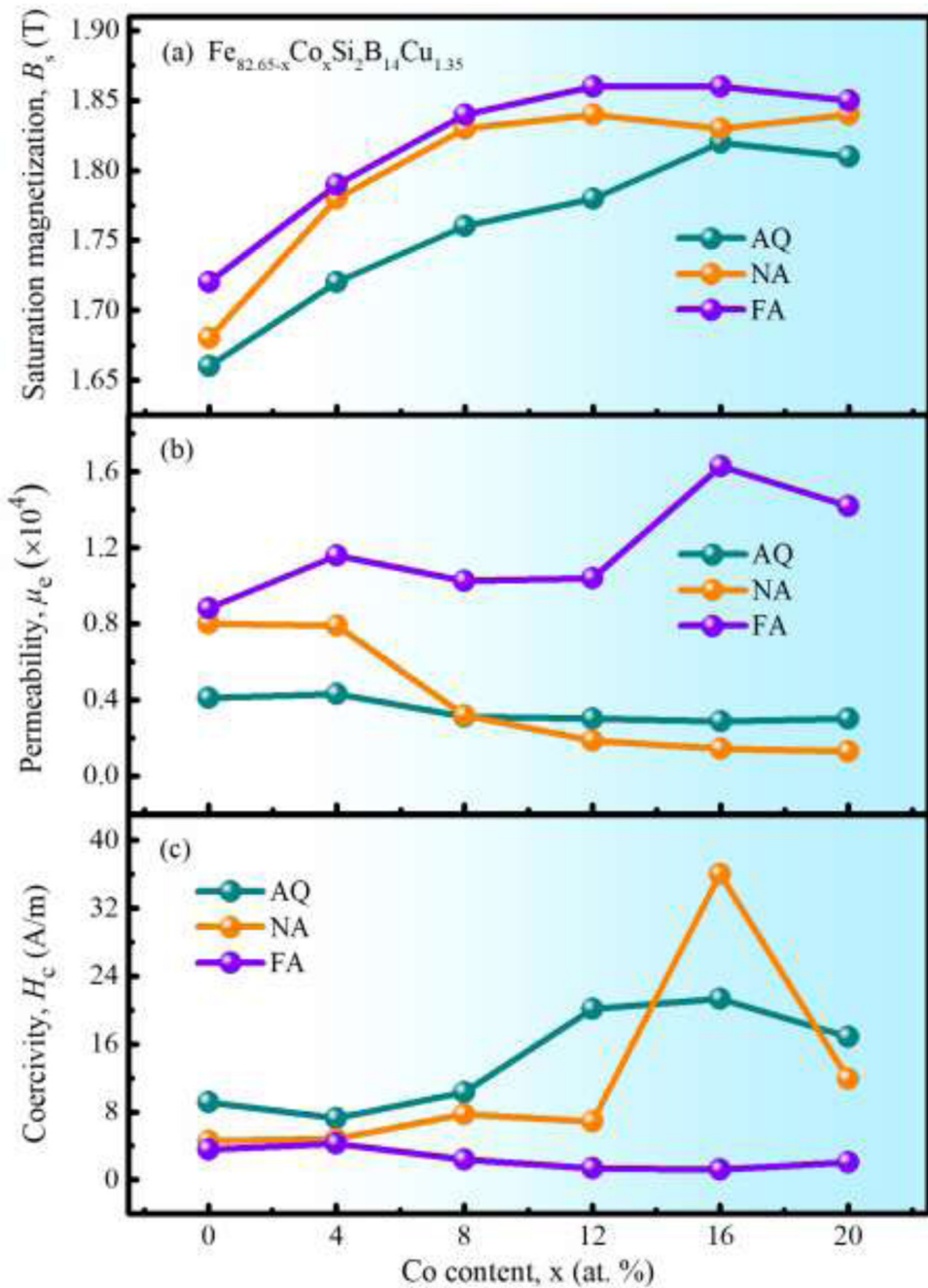


Fig. 2. The Co content dependence of (a) B_s , (b) μ_e and (c) H_c for $Fe_{82.65-x}CoxSi_2B_{14}Cu_{1.35}$ ($x = 0\text{--}20$) alloys treated by NA and FA at optimum condition, as well as the AQ state.

respectively. Note that the effective activation energy of primary crystallization determined from the heating rate dependence of crystallization first decreases with Co addition and increases with increasing Co content above $x=8$ (see details in Fig. S2 and Table S2). These results indicate a complex impact of Co addition on the local structure of the AAs and formation of α -(Fe, Co) phase.

To enhance the SMPs by modulating the short-range order (SRO), medium-range order (MRO) and magnetic domain structure, the AQ AAs were subjected to FA and NA in a vacuum at different temperatures (T_a) between 270 and 410 °C. For a given alloy treated by either NA or FA, H_c (μ_e) first decreases (increases) to a minimum (maximum) at a specific T_a (referred as the optimal T_a) and then increases (decreases) with further increasing T_a (see Fig. S4). Furthermore, the FA and NA impose markedly different influences on the SMPs, depending on the Co content. This can be seen clearly from Fig. 2, which manifests the B_s , μ_e and H_c as a function of Co content for the AQ and annealed AAs (NA or FA at the optimal T_a). The B_s of AQ alloys rises gradually with increasing Co content (Fig. 2(a)), showing the maximum at $x=16$, and then declines slightly, which suggests a transition from weak to strong ferromagnetism [24]. The increase of B_s after Co doping can be interpreted by the magnetic valence theory and was widely observed in FeCo-based AAs [25,26]. Upon NA, the structural relaxation leads to a denser atomic configuration, resulting in the increment of B_s for all the NA-treated alloys. It is worth noting that FA brings higher B_s than NA for all the AAs. The B_s of FA alloys increases obviously from 1.72 to 1.86 T with increasing Co content, and the highest value of $B_s \sim 1.86$ T is obtained in the $x=16$ alloy treated at 370 °C

ences on the SMPs, depending on the Co content. This can be seen clearly from Fig. 2, which manifests the B_s , μ_e and H_c as a function of Co content for the AQ and annealed AAs (NA or FA at the optimal T_a). The B_s of AQ alloys rises gradually with increasing Co content (Fig. 2(a)), showing the maximum at $x=16$, and then declines slightly, which suggests a transition from weak to strong ferromagnetism [24]. The increase of B_s after Co doping can be interpreted by the magnetic valence theory and was widely observed in FeCo-based AAs [25,26]. Upon NA, the structural relaxation leads to a denser atomic configuration, resulting in the increment of B_s for all the NA-treated alloys. It is worth noting that FA brings higher B_s than NA for all the AAs. The B_s of FA alloys increases obviously from 1.72 to 1.86 T with increasing Co content, and the highest value of $B_s \sim 1.86$ T is obtained in the $x=16$ alloy treated at 370 °C

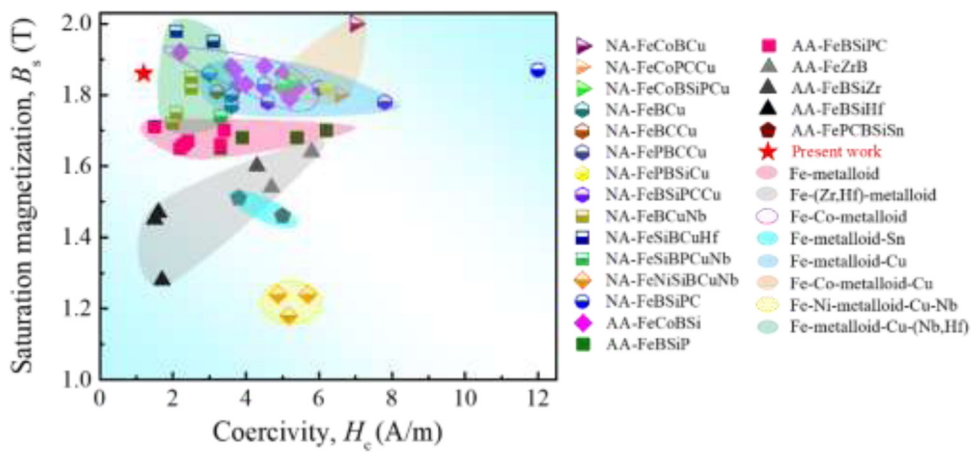


Fig. 3. B_s and H_c for the Fe-based amorphous and nanocrystalline soft magnetic alloys developed in the last ten years.

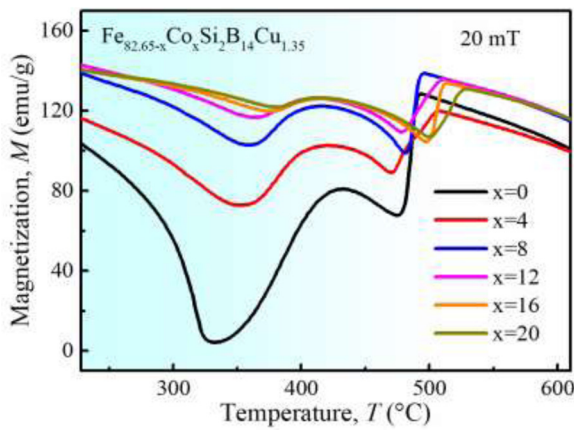


Fig. 4. The temperature dependence of magnetization for all the alloys.

for 15 min. In addition, we find that B_s can maintain an extremely high value above 1.82 T in a wide range of T_a (310–390 °C) for this alloy. Fig. 2(b) shows that NA only leads to a slight increase of μ_e for the $x = 0$ and 4 AAs but causes a slight reduction of μ_e for the alloys with $x > 8$. In contrast, FA increases μ_e considerably for all the alloys, especially the $x = 16$ and 20 alloys. Besides, NA and FA are almost equally effective in reducing H_c for the $x = 0$ and 4 alloys, as seen from Fig. 2(c). For the $x > 8$ alloys, FA reduces H_c much more effectively than NA, especially for the $x = 16$ alloy. Finally, an excellent combination of high μ_e of 16,300, low H_c of 1.2 A/m and super-high B_s of 1.86 T is observed in the $x = 16$ alloy after FA at 370 °C. Fig. 3 compares the B_s and H_c of present $x = 16$ alloy, and other typical high B_s Fe-based amorphous and nanocrystalline alloys reported [2,5,7–9,27–44]. It is evident that present AA exhibits super SMPs achieving good softness-magnetization balance, which can be regarded as one of the best soft magnetic alloys so far.

3.2. Magnetic transition and magnetic domain structure

To reveal the different effects of FA on the SMPs among the AAs with different Co contents as observed in Fig. 2, a set of thermomagnetic curves were measured and shown in Fig. 4. The magnetization decreases rapidly to almost zero with increasing temperature for the Co-free alloy, which indicates a typical ferromagnetic-paramagnetic transition. The T_c is determined to be 316 °C from the derivative of magnetization as a function of temperature (M - T curve). The subsequent rise of magnetization in the M - T curve

can be attributed to the precipitation of α -(Fe, Co) phase with higher magnetization, which also undergoes the ferromagnetic-paramagnetic transition with a drop of magnetization. Further sharp variations of magnetization at higher temperatures are related to the second crystalline phase. For the Co-contained alloys, the T_c increases with increasing Co content due to the stronger exchange interactions of Co-Co and Fe-Co pairs than Fe-Fe pairs [24–26]. But a complete ferromagnetic-paramagnetic transition cannot be observed in these alloys due to the occurrence of crystallization. T_c may exceed T_{x1} of the AAs with $x > 8$, and thus for $x = 0$ –8 with relatively low T_c , mainly a normal relaxation process associated with internal stress relief occurs when treated in the paramagnetic or weak ferromagnetic states. In contrast, the $x = 12$ –20 alloys with larger T_c than T_{x1} were in a ferromagnetic state during annealing. Thus, the SMPs of these $x > 8$ alloys are strongly influenced by the inner magnetic field [19].

To clarify the effect of the applied external and inner magnetic field on the magnetic structure at micrometer scale, the magnetic domains of the AQ, NA and FA $x = 16$ alloys were examined by MFM. The $x = 16$ alloy is chosen as a typical example since first it exhibits the most drastic difference in magnetic softness between the NA and FA states, and second it shows the best soft magnetic performance. As indicated in Fig. 5(a), both planar and maze domains are visible in the AQ sample, indicating the coexistence of stress-driven in-plane and perpendicular anisotropies. Thus, a relatively high applied magnetic field is necessary to drive the displacement of the domain walls, which along with the multipath rotation of the walls towards field direction during magnetization processes, leads to the poor SMPs. This can be further illustrated from the round hysteresis loop in Fig. 5(d), showing the magnetization process with inhomogeneous wall motion and rotational processes. After NA at 370 °C for 15 min, the domain structure becomes relatively homogeneous and is dominated by the planar type associated with a low-stress state. But rugged edges/interfaces and irregular arrangement of the domains are observed, indicating a strong pinning effect, which generates a squared loop with high remanence and large H_c as depicted in Fig. 5(d). In contrast, the FA alloy shows regular planar domains with large width and smooth edge (Fig. 5(c)), which are neatly aligned along the direction of the applied magnetic field. And there is no obvious pinning site, which facilitates an unobstructed movement of the domains and leads to enhanced magnetic softness, as illustrated by the hysteresis loop with a high squareness ratio and low H_c . These results indicate the significant role of interaction between applied and inner magnetic fields on soft magnetic behaviors. In the NA sample, the inner magnetic field (in its ferromagnetic state) stabilizes the irregular arrangement of magnetic domains during

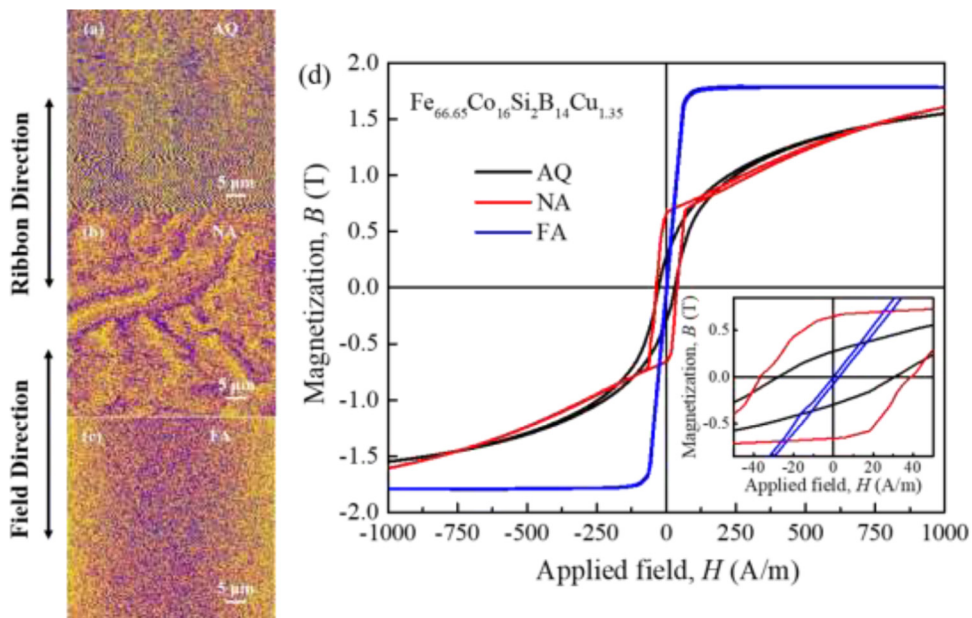


Fig. 5. Magnetic domain patterns of $\text{Fe}_{66.65}\text{Co}_{16}\text{Si}_2\text{B}_{14}\text{Cu}_{1.35}$ ribbon samples at (a) AQ, (b) NA and (c) FA states. (d) Hysteresis loops of $\text{Fe}_{66.65}\text{Co}_{16}\text{Si}_2\text{B}_{14}\text{Cu}_{1.35}$ ribbon samples at AQ, NA and FA states. Partial enlarged plot is given as the inset.

annealing and enhances the complex magnetic anisotropy [19], which deteriorates the magnetic softness. Similar increased H_c by NA has been observed in $x=8, 12, 20$ alloys (Fig. S4). FA can remove the negative influence of the inner field and reorganize the magnetic domain structure, which increases the longitudinal anisotropy and enhances the SMPs of the $x=16$ alloy.

3.3. Atomic structure change induced by NA/FA

Up to now, it is unclear how the different SMPs among the AQ and NA/FA states correlate with atomic structure due to the difficulty of directly investigating the subtle structure change. Conventional XRD usually cannot detect the slight difference between AQ and NA/FA [19]. From indirect magnetic relaxation measurement, it was suggested that FA might reduce the number of mobile defects [45]. Recently, it was found that FA at 1 T promoted the formation of spherical symmetry clusters in an Fe-Si-B AA, possibly relating to the enhanced SMPs [20]. To shed light on the structural origin of different SMPs between NA and FA states, DSC, synchrotron XRD and HRTEM experiments were conducted. Fig. 6(a) shows the DSC curves of the AQ, NA and FA alloys (treated at optimal T_a). An apparent shallow hump can be observed below T_{x1} in the DSC curve of the AQ alloy, arising from the release of remnant excess enthalpy. After NA this exothermic hump reduces significantly due to gradual annihilation of the quench-in free volume. Interestingly, the FA alloy shows more energy release during annealing than the NA sample, which means that FA promotes the system to a deeper energy state basin in the potential energy landscape. And the T_{x1} also increases slightly after FA compared with that of the NA alloy, which implies that the additional local structural arrangement by applied field further enhances the thermal stability against crystallization. In addition, as shown in Fig. 6(b), the synchrotron XRD patterns of the FA and NA samples show little change of the first diffraction peak (Q_1) position and a slight change of the peak shape. This suggests that the applied magnetic field causes additional arrangement of MRO without affecting the local density [46].

Fig. 7(a–c) presents the TEM images and corresponding fast Fourier transformation (FFT) patterns of the AQ, NA and FA (annealed at 370 °C) $x=16$ alloys. The bright-field TEM images and

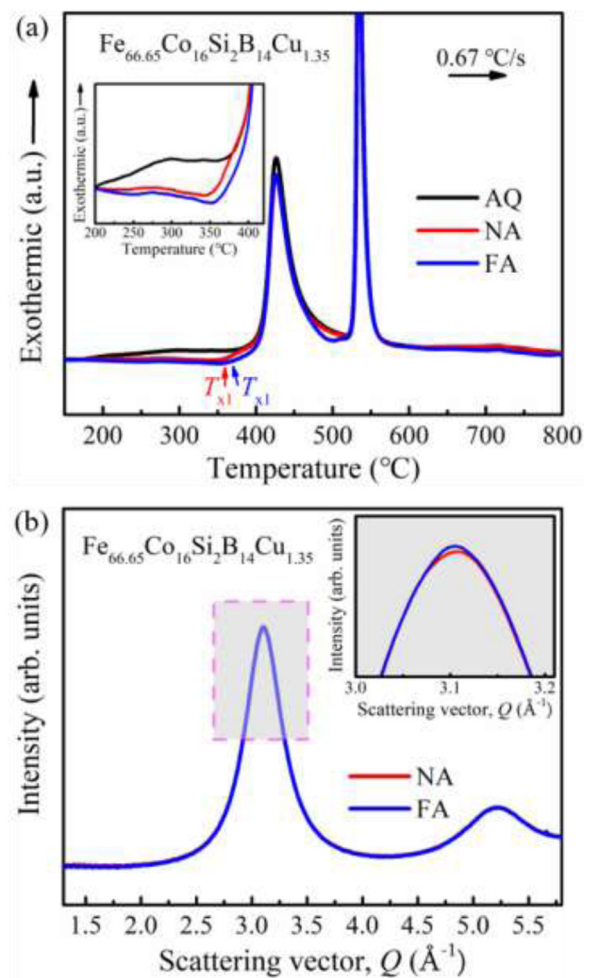


Fig. 6. (a) DSC curves for $\text{Fe}_{66.65}\text{Co}_{16}\text{Si}_2\text{B}_{14}\text{Cu}_{1.35}$ ribbons at AQ, NA and FA states. The inset demonstrates a partial enlargement. (b) Synchrotron XRD of $\text{Fe}_{66.65}\text{Co}_{16}\text{Si}_2\text{B}_{14}\text{Cu}_{1.35}$ ribbon samples treated by NA and FA. The inset shows the enlarged image of the gray area.

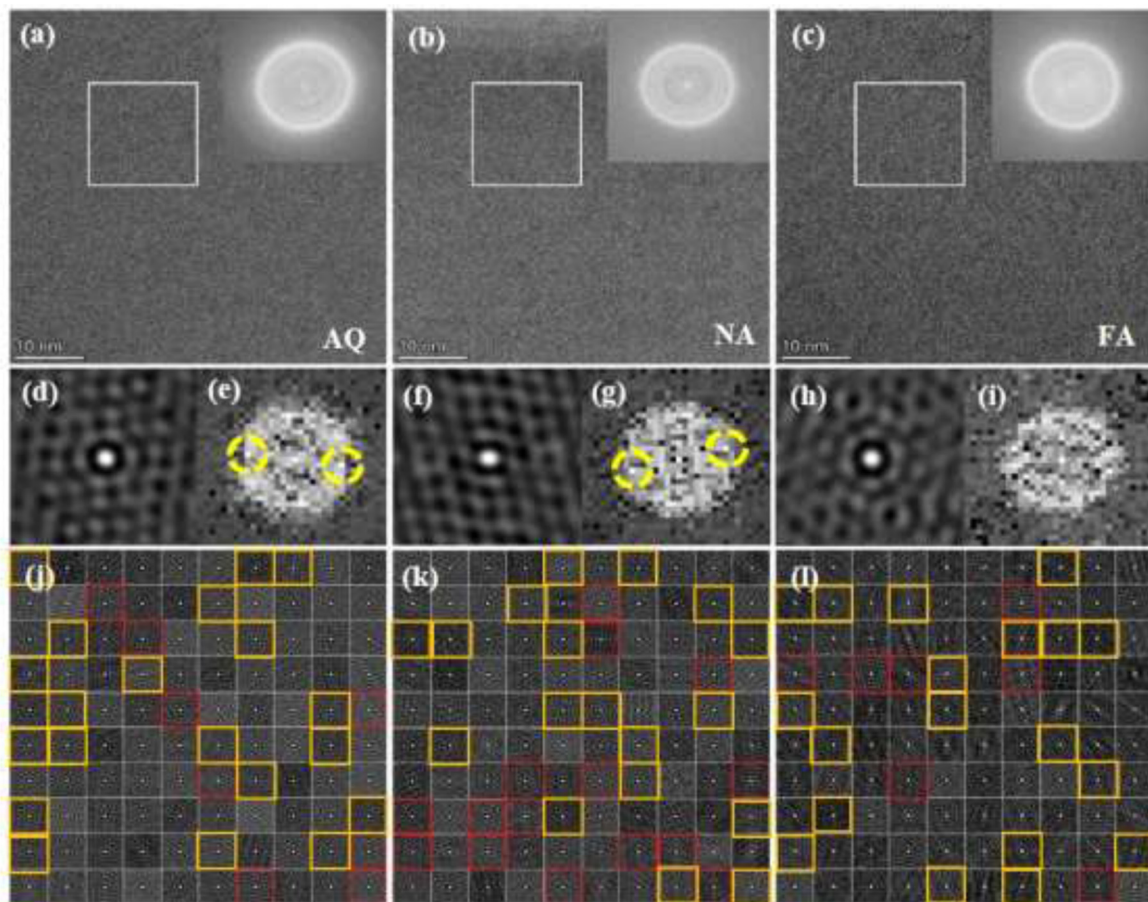


Fig. 7. The HRTEM images and the corresponding FFT patterns for $\text{Fe}_{66.65}\text{Co}_{16}\text{Si}_2\text{B}_{14}\text{Cu}_{1.35}$ ribbons at (a) AQ, (b) NA and (c) FA states. Representative auto-correlation images of typical cells with (d, f) crystal-like and (h) typical most disordered orders, and the corresponding FFT patterns (e, g, i). (j–l) Auto-correlation maps for the selected parts of the HRTEM images of (a–c). The cells showing crystal-like order and the most disordered feature are marked by red and orange rectangles, respectively.

FFT patterns all reveal a completely amorphous structure. A slight difference of the FFT patterns can be observed among the three alloys. The NA alloy shows more shallow diffraction rings than the AQ alloy implying its more ordered structure, and the FA alloy has the most minor ring features indicating its most disordered structure. More details can be revealed from the 2D auto-correlation map, from which one can quantify the areal fraction of MRO with crystal-like order in the alloys (examples are shown in Fig. 7(d–g)) [47]. The square areas selected in Fig. 7(a–c) are divided into 100 square cells, each of which has a size of 2.0 nm, the typical size of MRO in AAs [48,49]. From the 2D auto-correlation images in Fig. 7(j–l), the total area fraction of the crystal-like cells is about $8\% \pm 1\%$, $15\% \pm 1\%$, $7\% \pm 1\%$ for the AQ, NA and FA alloys. But the area fraction of the most disordered clusters (Fig. 7(h, i)) is almost the same ($\sim 20\% \pm 1\%$) for all the alloys. Accordingly, different from the promoted structure ordering of clusters by NA, structure ordering is significantly impeded by FA, which possibly interprets the enhanced effective activation energy of primary crystallization and increased T_{x1} . To explore the possible nanoscale chemical or density fluctuations in present AAs, high-resolution Z-contrast HAADF-STEM measurement was performed. The AQ sample shows heterogeneous contrast with dark and bright areas in Fig. 8(a) and (c), as a result of an inhomogeneous distribution of density and/or chemistry. The STEM mappings of elements show a relatively homogeneous distribution, and a visible correlation between chemical variation and heterogeneity (in Fig. 8(b)) cannot be detected. Thus, the dark-bright contrast in the HAADF-STEM image mainly arises from the mass density variation, as indicated in a Zr-based metallic glass

[48]. After NA, the inhomogeneous contrast of the HAADF-STEM decreases slightly (Fig. 8(d) and (f)), indicating a more homogeneous microstructure in the NA AA. Moreover, the intensity profiles taken from a diagonal line of the Cu mappings reveals the most uniform distribution of Cu in the FA alloy and the most heterogeneous in the AQ alloy. These results indicate that the external field during annealing can further promote atomic arrangements to a more homogeneous atomic configuration. The more uniform structure with fewer defects, suppressed crystal-like orders and less Cu clustering contribute structurally to the superb SMPs in the FA-treated alloy.

Next, we discuss briefly the structural origin of the deterioration of FA on SMPs starting from ~ 375 °C for the $x=16$ AA. Fig. 9(a,b,e,f) compares the TEM images, selected area electron diffraction (SAED) and FFT patterns (the insets) of the NA and FA specimens, from which a few nanocrystalline grains embedded in the residual amorphous matrix can be revealed. Note that conventional XRD (not shown here) reveals amorphous structure of this annealed alloy, indicating its quite small volume fraction. Statistical analysis reveals that the α -(Fe, Co) grains in the NA sample have a size range of 5–20 nm with 10 nm in average. In contrast, α -(Fe, Co) grains in the FA alloy have a smaller average grain size of 5 nm. This may imply that the applied magnetic field retards diffusion of atoms during annealing, as long-range atomic diffusion is necessary for the growth of crystals. It was found that the diffusion of carbon in γ -Fe was retarded by a magnetic field [50]. In addition, different from the irregular-shape grains in the NA alloy, strip-like grains with preferred arrangement orientation are observed in the

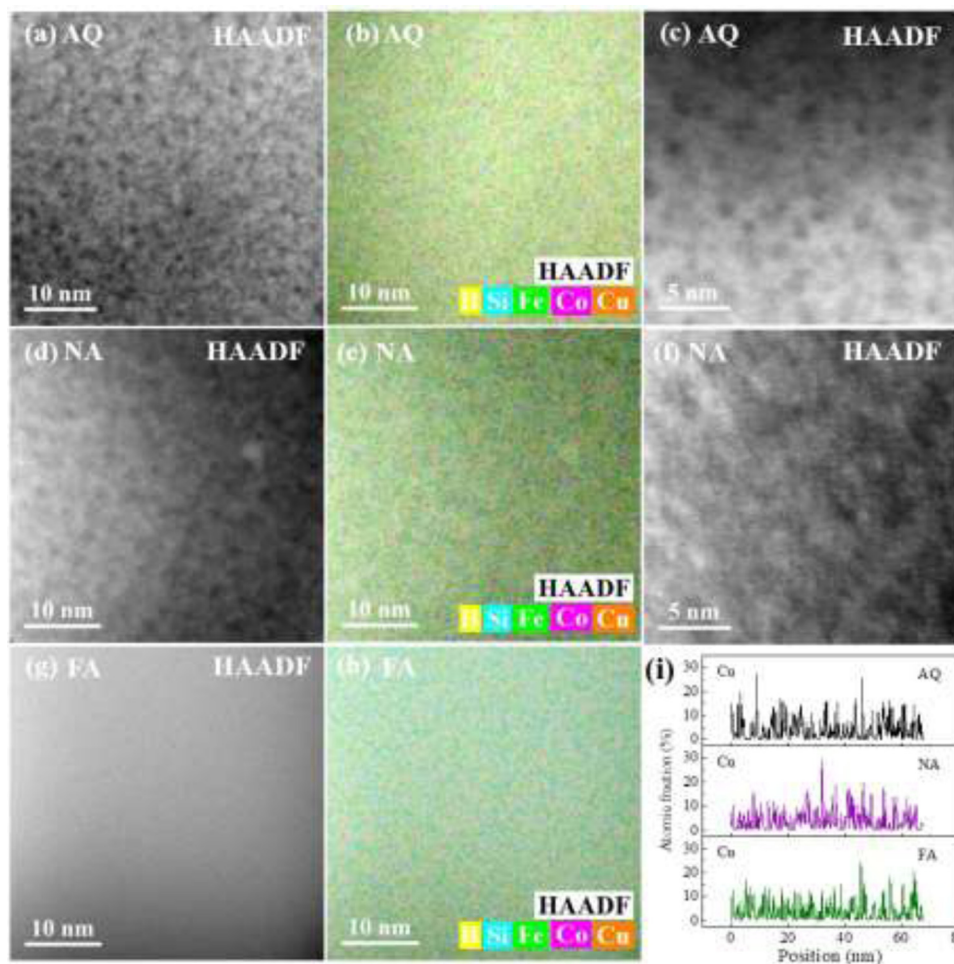


Fig. 8. HAADF STEM images and the corresponding mappings of AQ and annealed $\text{Fe}_{66.65}\text{Co}_{16}\text{Si}_2\text{B}_{14}\text{Cu}_{1.35}$ at 370 °C for 15 min.

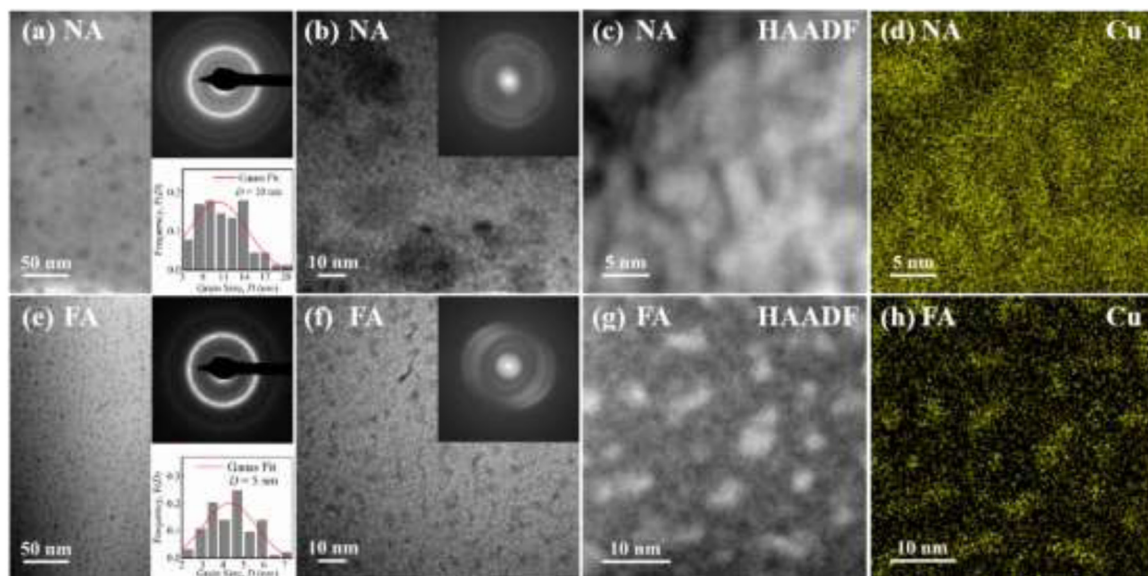


Fig. 9. The bright-field TEM images, SAED patterns, grain size distribution, HAADF STEM images and corresponding EDS mappings of Cu element for samples treated by NA and FA at 375 °C for 5 min.

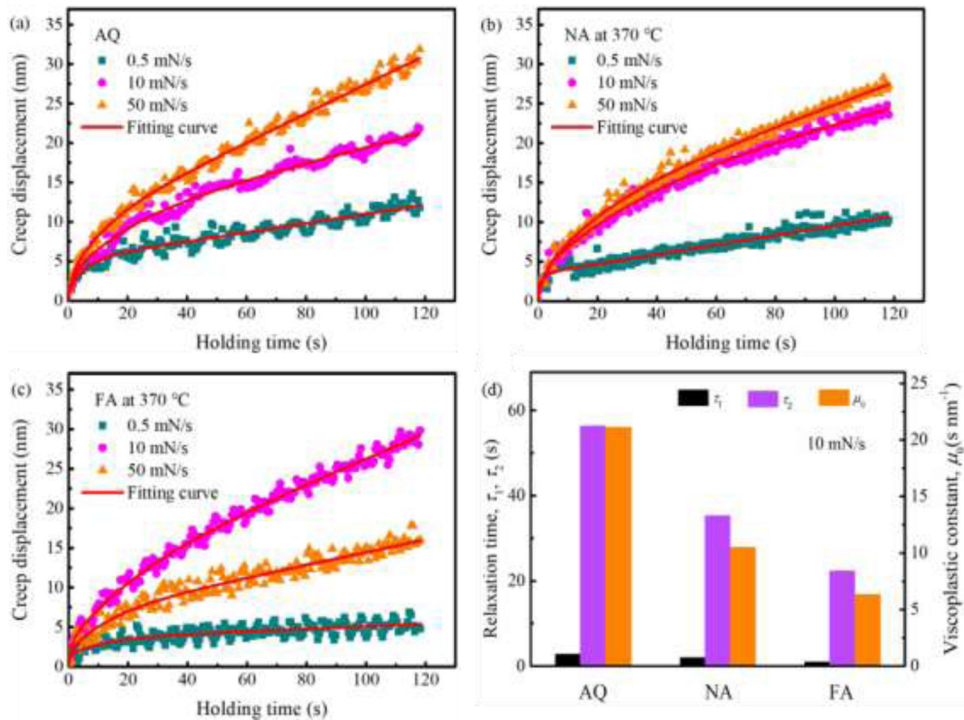


Fig. 10. Experimental and fitting creep curves of the $\text{Fe}_{66.65}\text{Co}_{16}\text{Si}_2\text{B}_{14}\text{Cu}_{1.35}$ ribbons at (a) AQ, (b) NA, and (c) FA states at different loading rates. (d) The histogram of the fitting parameters of creep curves for the $\text{Fe}_{66.65}\text{Co}_{16}\text{Si}_2\text{B}_{14}\text{Cu}_{1.35}$ ribbons at AQ, NA and FA states based on the Maxwell-Voigt model.

FA alloy, indicating a significant impact of FA on the atomic arrangement and diffusion. In the HAADF-STEM image of the NA sample (Fig. 9(c)) dark and bright regions can be detected, which correspond to the Cu-poor and Cu-rich regions (Fig. 9(d)), respectively. In contrast, more remarkable Cu-cluster formation with diameter of 2–6 nm occurs in the FA alloys, which leads to more obvious bright-dark contrast in the HAADF-STEM image (Fig. 9(e,g,h)). These Cu clusters serve as nuclei to promote the formation of fine nanocrystals in the FA alloy [51,52]. But the Fe element exhibits relatively homogeneous distribution, which could be due to similar Fe contents in the amorphous matrix and α -(Fe, Co) nanocrystals. Therefore, the formation of nanocrystals increases the magneto-crystalline anisotropy significantly, which can overcome the FA-induced magnetic anisotropy and increase the H_c ($\sim 8.8 \text{ A/m}$). This result clarifies that even if the α -(Fe, Co) fraction is quite small, it is still the random anisotropy model that determines the soft magnetic mechanism of two-phase nanocrystalline systems [53].

3.4. Nanoindentation creep deformation

Creep deformation was investigated by nanoindentation to further comprehend the effect of FA on the heterogeneous structural arrangements at nanometer scale. Fig. 10(a–c) shows the holding time dependence of the creep displacement of the alloys. The maximum creep displacement of the AQ alloy increases from 12.1 to 37.6 nm when increasing the loading rate from 0.5 to 50 mN/s. These values are similar to those of other MGs [54,55]. After NA at 370°C , the maximum creep displacements at loading rates of 0.5 and 50 mN/s decrease to 9.0 and 20.6 nm, respectively, due to the denser structure. For the FA alloy, this displacement is determined to be 5.7 and 19.4 nm at loading rates of 0.5 and 50 mN/s, respectively, demonstrating a less pronounced creep deformation after FA. To further understand the creeping process, the Maxwell-Voigt model containing Maxwell and Kelvin units is used to analyze the creep curves [56]. After assuming that the sudden elastic strain before the first stage of anelastic deformation is zero, the

creep displacement can be described by [57]:

$$H(t) = h_1(1 - e^{-t/\tau_1}) + h_2(1 - e^{-t/\tau_2}) + t/\mu_0 \quad (1)$$

where t is the holding time, h_i is the indentation depth and τ_i is the characteristic relaxation time of the i -th anelastic Kelvin unit, and μ_0 is a constant of the Maxwell dashpot (proportional to the viscosity coefficient). As shown in Fig. 10, the creep curves of all the AQ, NA and FA alloys can be fitted very well with Eq. (1) containing two Kelvin units and one Maxwell unit. For all the alloys, both h_1 and h_2 increase at first and then decreases with increasing loading rate. The τ_1 , τ_2 and μ show slight differences among the AQ, NA and FA alloys at 0.5 and 50 mN/s, but noticeable differences can be observed at 10 mN/s as indicated in Fig. 10(d). All the τ_1 , τ_2 and μ decrease as the sample changes from AQ, NA to FA states. Thus, applying an external field during annealing further reduces the viscosity coefficient of the Maxwell dashpot and characteristic relaxation times of both anelastic Kelvin units.

Moreover, the isothermal relaxation time spectra are analyzed by using the following equation [54]:

$$L(\tau) = \left[\sum \left(1 + \frac{t}{\tau_i} \right) \frac{h_i}{\tau_i} e^{-\frac{t}{\tau_i}} \right] \frac{A_0}{P_0 h_{in}} t|_{t=2\tau} \quad (2)$$

where L represents the spectrum intensity, h_{in} represents the maximum indentation depth, and A_0/P_0 represents the inverse of hardness. Fig. 11(a) shows the typical relaxation spectra of AQ alloy obtained at loading rates of 0.5, 10 and 50 mN/s. It can be seen clearly that both the intensity and characteristic times of the relaxation peaks increase when increasing the loading rate from 0.5 to 10 mN/s. Thus, more defects with longer relaxation time can be activated during deformation at a larger loading rate, which is in accordance with that observed in other AAs [58]. However, further increasing the loading rate to 50 mN/s leads to a decrease in both the characteristic times and intensity of the relaxation peaks. These abnormal behaviors may arise from the saturation effect of the activated defects at a loading rate of 50 mN/s. Similar loading rate-dependent behavior has been observed in the NA and FA

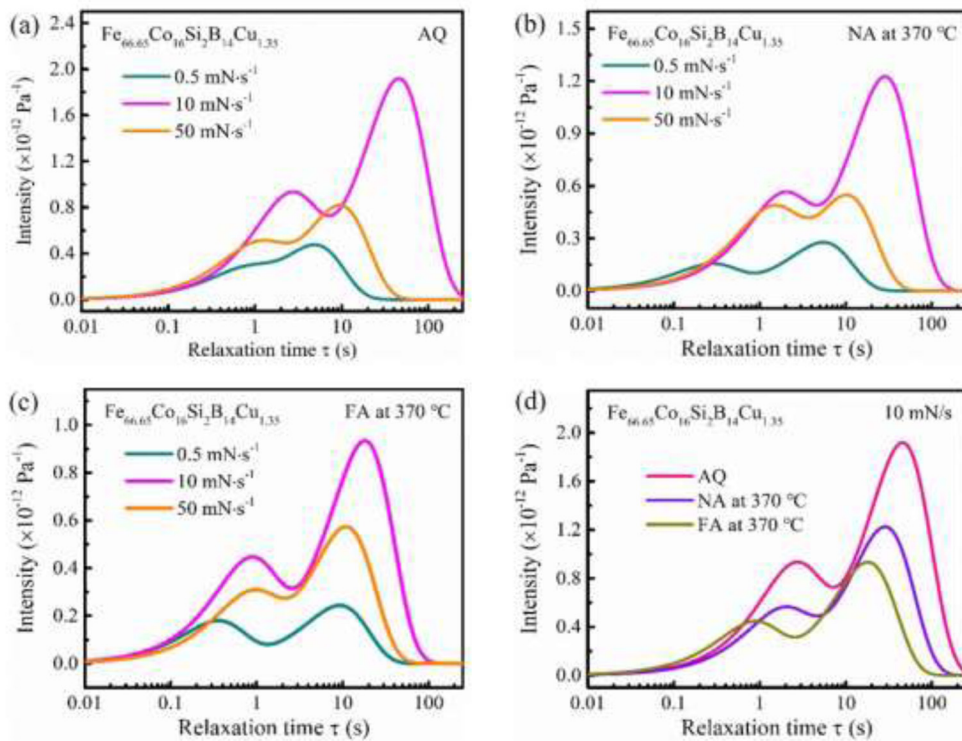


Fig. 11. The relaxation spectra of $\text{Fe}_{66.65}\text{Co}_{16}\text{Si}_2\text{B}_{14}\text{Cu}_{1.35}$ ribbons at (a) AQ, (b) NA, and (c) FA states under different loading rates with a maximum load of 80 mN. (d) The relaxation spectra of $\text{Fe}_{66.65}\text{Co}_{16}\text{Si}_2\text{B}_{14}\text{Cu}_{1.35}$ ribbons at AQ, NA and FA states under the loading rate of 10 mN/s .

alloys as indicated in Fig. 11(b) and (c). Fig. 11(d) compares the relaxation spectra of AQ, NA and FA alloys obtained at a loading rate of 10 mN/s . All the intensity and characteristic times of both peaks at 10 mN/s decrease after NA at 370 °C, which indicates the significant reduction of both types of defects responsible for the relaxation peaks due to the stress relief and denser atomic packing. Interestingly, after FA the intensity and characteristic time of both relaxation peaks further decrease compared with that of NA alloy, which implies that fewer defects with shorter relaxation time were stimulated (for both relaxation peaks) in the FA alloy.

It has been widely accepted that AAs have considerable diversity in short-to-medium-range orders, possessing liquid-like and solid-like regions [54,57]. The heterogeneous atomic configurations at different length scales play a significant role in glass formation, relaxation and deformation of AA systems [48,59]. The two-phase model of MGs with the liquid-like region (free volume zone) and the solid-like region is usually used to characterize the two anelastic relaxation events [60]. It was suggested that the first peak with a short relaxation time of the relaxation spectra in Fig. 11 is related to the activation of defects in the solid-like regions with a relatively strong atomic bonding, while the second one with defects in the liquid-like region with weaker bonding. The increase of intensity and relaxation time with increasing loading rate from 0.5 to 10 mN/s in all the AAs implies that more defects in liquid-like and solid-like regions are stimulated at a higher loading rate. This is in accordance with the observation in the Fe- and Zr-based AAs [54,55]. The weakest intensity of both peaks in the relaxation spectra of FA alloy in Fig. 11(d) indicates that both liquid-like and solid-like defects activated during deformation reduce significantly after FA. And the liquid-like defects show more significant reduction in their number than the solid-like defects. Besides, the shift of both relaxation peaks to lower time implies that the size of both types of defects decreases in the FA alloy. Therefore, one can deduce that FA homogenizes the local structure via reducing the number and

size of both liquid-like and solid-like defects, which modifies the creep deformation and SMP significantly in present alloy.

At last, we discuss the effect of magnetic and structural heterogeneities on SMPs of the AAs. Present AA system has pronounced local structural heterogeneity arising from the positive heats of mixing of Fe-Cu pair (13 kJ/mol) and Co-Cu pair (6 kJ/mol) [61]. This results in a considerable diversity in the local atomic configurations around Fe atoms, which leads to significant fluctuations of exchange energies and local anisotropy (from magnetic heterogeneity). Besides, the Co doping introduces Co-Co and Fe-Co pairs having different exchange integrals with the Fe-Fe pairs, introducing additional magnetic heterogeneity. Since H_c is sensitive to structural/magnetic heterogeneity (such as free volume, residual stress and inhomogeneous magnetic structure), good magnetic softness is not obtained in all the AQ Co-doping AAs. And next, we discuss the bizarre effects of enhancing the B_s considerably but deteriorating the magnetic softness obviously upon Co addition as observed here and in other systems [25,26]. The significant increase of B_s upon Co alloying originates from the enhanced exchange interaction and promoted electron transfer into the spin-up 3d band of Fe atom [62]. While the markedly worsened softness for the $x>8$ alloys could relate to a combination of enhanced magnetic heterogeneity (giving rise to more pinning centers for magnetic domains) and increased local magnetic anisotropy (see the irregularly mussy wide and narrow magnetic domains and round magnetic loop in Fig. 5(d)).

Usually, NA below the crystallization temperature can lead to the denser atomic packing, structural homogenization and stress relief, which result in a slight decrease of H_c and an increase of B_s (as observed in most alloys investigated here). However, the magnetic softness becomes worse after NA in the $x=16$ alloy. We argue that this is related to the complicated inner magnetic field, which strongly affects the atomic arrangement and magnetic homogenization processes during annealing. The HAADF-STEM image

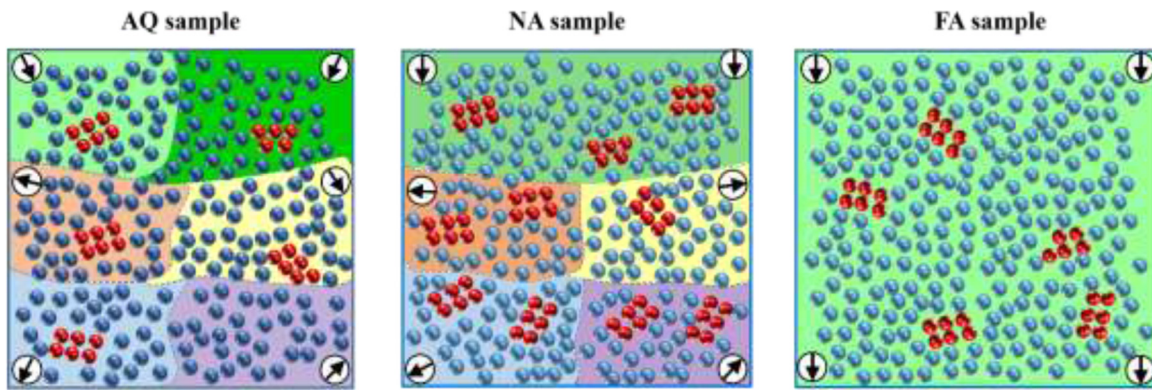


Fig. 12. Schematic diagram of magnetic domain and atomic structures of $\text{Fe}_{66.65}\text{Co}_{16}\text{Si}_2\text{B}_{14}\text{Cu}_{1.35}$ AAs in the AQ, NA and FA states. The blue balls denote the atoms forming completely disordered microstructure, and the red balls denote the atoms forming crystal-like clusters. Groups of atoms with different background colors refer to different magnetic domains, where the fluctuations of the easy magnetization direction are indicated by the arrows.

in Fig. 8(d) reveals that this inner magnetic field tends to slow down the homogenization process during annealing, as seen from the slight change of the contrast and increased crystal-like clusters. Thus, the heterogeneity nature composed of weak/medium/strong ferromagnetic regions (clusters) with different exchange couplings between clusters and diverse local magnetic anisotropy is not improved significantly. And the increased crystal-like clusters introduce more structure defects, which should impede the effective arrangement of Fe-Fe (Co) pairs and pin the domain walls. Furthermore, the relaxation during NA may further enhance the magnetic heterogeneity owing to the inhomogeneous thermal strains and complicated inner magnetic field, which causes increased local magnetic anisotropy and worse SMPs as also observed in other AA systems [19]. The different magnetic domain and atomic structures between the AQ and NA AAs are presented in Fig. 12. Interestingly, FA can provide an effective/promising pathway overcoming the negative effect of the inner magnetic field and solving the dilemma about the softness-magnetization trade-off. In addition to homogenizing locally the magnetic domain structure (as illustrated in Fig. 12), FA can rearrange the local structures into a more homogeneous configuration (see Fig. 8(g)) with less crystal-like clusters, which considerably reduces the magnetic-domain pinning centers. Besides, the reduced structural and magnetic heterogeneities by FA can be further illustrated from the relaxation spectra. The liquid-like and solid-like defects responsible for the creep deformation should have different exchange coupling interactions from their local surroundings, which increases the heterogeneity of exchange-coupling energy and can be considered as magnetic defects to pin the domain walls. In some nanomagnets, it was found that pinning took place at the interface regions with weak exchange coupling [63]. It is possible that pinning prefers to occur in the liquid-like regions with weak exchange interaction in the amorphous matrix, which but needs further exploration. The suppressed defect activation in relaxation spectra of Fig. 11(d) means that FA significantly homogenizes the exchange coupling interactions among clusters and reduces the magnetic defects (as the pinning centers). And this process facilitates the movement and rotation of the domain wall coherently, leading to a large reduction of H_c from 23.1 A/m in AQ state to 1.2 A/m in FA state. In addition, due to the structural and magnetic heterogeneities, clusters with rich or poor Fe-Fe (Co) pairs coexist in the AQ alloy, which should arrange differently during NA and FA. The structure arrangement under inhomogeneous thermal strain and external field may promote the development of a higher level of Fe-Fe (Co) pairs with preferred orientation along the direction of the external field. This results in enhanced exchange interactions among Fe-Fe (Co) pairs and improved B_s as seen in Fig. 2, and correlates with the field-induced

uniaxial anisotropy along the ribbon axis as well. In the Fe-Co-Ni-B nanocrystalline alloys showing improved SMPs after FA, magnetic atoms pair ordering was suggested to contribute to the field-induced magnetic anisotropy [64]. More investigations are needed in the future to clarify this issue.

4. Conclusion

We successfully achieve a superior softness-magnetization combination in the field-annealed $\text{Fe}_{66.65}\text{Co}_{16}\text{Si}_2\text{B}_{14}\text{Cu}_{1.35}$ AA. A much larger B_s (1.86 T) and a smaller H_c (1.2 A/m) than those of the commercial Fe-based AAs ($B_s \sim 1.56$ –1.63 T and $H_c \sim 2$ A/m) are attractive for industrial application. Besides, this AA system takes advantage of better industry manufacturability than the P and/or C contained AAs and nanocrystalline alloys. Moreover, comprehensive effects of FA on structural and magnetic heterogeneities at different length scales and on SMPs have been revealed, including formation of uniform magnetic domains at micrometer scale, homogenization of structure at SRO and MRO scales, reducing both the liquid-like and solid-like defects at nanometer scale, and suppressing the structural ordering at MRO. These results shed new light on the correlation between structural/magnetic heterogeneities and magnetic/mechanical properties and guide the development of novel soft magnets with excellent softness-magnetization balance.

Declaration of Competing Interest

The authors declare no conflicts of interest.

Acknowledgment

This work was financially supported by the National Natural Science Foundation of China (Nos. 51631003 and 51971061).

Data availability

The data that support the findings of this study are available from the corresponding author upon reasonable request.

Supplementary materials

Supplementary material associated with this article can be found, in the online version, at doi:10.1016/j.jmst.2021.11.038.

References

- [1] J.M. Silveyra, E. Ferrara, D.L. Huber, T.C. Monson, *Science* 362 (2018) eaao0195.
- [2] L. Shi, K. Yao, *Mater. Des.* 189 (2020) 108511.

- [3] D. Azuma, N. Ito, M. Ohta, *J. Magn. Magn. Mater.* 501 (2020) 166373.
- [4] B. Shen, A. Inoue, C. Chang, *Appl. Phys. Lett.* 85 (2004) 4911–4913.
- [5] X. Liang, A. He, A. Wang, J. Pang, C. Wang, C. Chang, K. Qiu, X. Wang, C.T. Liu, *J. Alloy. Compd.* 694 (2017) 1260–1264.
- [6] K.F. Yao, L.X. Shi, S.Q. Chen, Y. Shao, N. Chen, J.L. Jia, *Acta Phys. Sin.* 67 (2018) 016101.
- [7] P. Chen, A. Wang, C. Zhao, A. He, G. Wang, C. Chang, X. Wang, C.T. Liu, *Sci. China Phys. Mech. Astron.* 60 (2017) 106111.
- [8] F. Wang, A. Inoue, Y. Han, F.L. Kong, S.L. Zhu, E. Shalaan, F. Al-Marzouki, A. Obaid, *J. Alloy. Compd.* 711 (2017) 132–142.
- [9] M. Shi, Z. Liu, T. Zhang, *J. Mater. Sci. Technol.* 31 (2015) 493–497.
- [10] K. Suzuki, A. Makino, A. Inoue, T. Masumoto, *J. Appl. Phys.* 70 (1991) 6232–6237.
- [11] K. Xu, H. Ling, Q. Li, J. Li, K. Yao, S. Guo, *Intermetallics* 51 (2014) 53–58.
- [12] R.K. Roy, A.K. Panda, A. Mitra, *J. Magn. Magn. Mater.* 418 (2016) 236–241.
- [13] A. Nabais, J.C. Faugières, J.F. Rialland, R. Bonnefille, *Rev. Phys. Appl.* 19 (1984) 1–5.
- [14] C. Zhao, A. Wang, A. He, S. Yue, C. Chang, X. Wang, R.W. Li, *J. Alloy. Compd.* 659 (2016) 193–197.
- [15] I. Škorvánek, J. Marcin, J. Turčanová, J. Kováč, P. Švec, *J. Alloy. Compd.* 504S (2010) S135–S138.
- [16] D. Mishra, P. Saravanan, A. Perumal, A. Srinivasan, *J. Appl. Phys.* 109 (2011) 07A306.
- [17] P. Marín, A. Hernando, *Appl. Phys. Lett.* 94 (2009) 122507.
- [18] M. Liu, Z. Wang, Y. Xu, *IEEE Trans. Magn.* 51 (2015) 2004704.
- [19] C. Zhao, A. Wang, S. Yue, T. Liu, A. He, C. Chang, X. Wang, C.T. Liu, *J. Alloy. Compd.* 742 (2018) 220–225.
- [20] C. Wang, Z. Wu, X. Feng, Z. Li, Y. Gu, Y. Zhang, X. Tan, H. Xu, *Intermetallics* 118 (2020) 106689.
- [21] J. Xu, Y. Yang, Q. Yan, G. Xiao, T. Luo, C. Fan, *Scr. Mater.* 179 (2020) 6–11.
- [22] M. Ohta, Y. Yoshizawa, *Appl. Phys. Lett.* 91 (2007) 062517.
- [23] M. Ohta, Y. Yoshizawa, *J. Phys. D Appl. Phys.* 44 (2011) 064004.
- [24] A. Williams, V. Moruzzi, A. Malozemoff, K. Terakura, *IEEE Trans. Magn.* 19 (1983) 1983–1988.
- [25] S. Bhattacharya, E.A. Lass, S.J. Poon, G.J. Shiflet, M. Rawlings, M. Daniil, M.A. Willard, *J. Appl. Phys.* 111 (2012) 063906.
- [26] R.C. O’Handley, R. Hasegawa, R. Ray, C.P. Chou, *Appl. Phys. Lett.* 29 (1976) 330–332.
- [27] F. Wang, A. Inoue, Y. Han, S.L. Zhu, F.L. Kong, E. Zanaeva, G.D. Liu, E. Shalaan, F. Al-Marzouki, A. Obaid, *J. Alloy. Compd.* 723 (2017) 376–384.
- [28] H. Li, A. Wang, T. Liu, P. Chen, A. He, Q. Li, J. Luan, C.T. Liu, *Mater. Today* 42 (2021) 49–56.
- [29] A. Wang, C. Zhao, H. Men, A. He, C. Chang, X. Wang, R.W. Li, *J. Alloy. Compd.* 630 (2015) 209–213.
- [30] F.L. Kong, C.T. Chang, A. Inoue, E. Shalaan, F. Al-Marzouki, *J. Alloy. Compd.* 615 (2014) 163–166.
- [31] H. Zheng, L. Zhu, S.S. Jiang, Y.G. Wang, F.G. Chen, *J. Alloy. Compd.* 834 (2020) 155068.
- [32] A.D. Setyawan, K. Takenaka, P. Sharma, M. Nishijima, N. Nishiyama, A. Makino, *J. Appl. Phys.* 117 (2015) 17B715.
- [33] Y. Meng, S. Pang, C. Chang, X. Bai, T. Zhang, *J. Magn. Magn. Mater.* 523 (2021) 167583.
- [34] R. Parsons, Z. Li, K. Suzuki, *J. Magn. Magn. Mater.* 485 (2019) 180–186.
- [35] Z. Li, A. Wang, C. Chang, Y. Wang, B. Dong, S. Zhou, *J. Alloy. Compd.* 611 (2014) 197–201.
- [36] G.T. Xia, Y.G. Wang, J. Dai, Y.D. Dai, *J. Alloy. Compd.* 690 (2017) 281–286.
- [37] R. Parsons, B. Zang, K. Onodera, H. Kishimoto, A. Kato, K. Suzuki, *J. Alloy. Compd.* 723 (2017) 408–417.
- [38] M. Xiao, L. Zheng, L. Zhou, H. Yu, G. Wang, D. Zeng, *J. Non Cryst. Solids* 556 (2021) 120560.
- [39] B. Zang, R. Parsons, K. Onodera, H. Kishimoto, A. Kato, A.C.Y. Liu, K. Suzuki, *Scr. Mater.* 132 (2017) 68–72.
- [40] Y. Geng, Y. Wang, Z. Wang, J. Qiang, H. Wang, C. Dong, O. Tegus, *Mater. Des.* 106 (2016) 69–73.
- [41] M. Shi, Z. Liu, T. Zhang, *J. Magn. Magn. Mater.* 378 (2015) 417–423.
- [42] T. Warski, A. Radon, P. Zackiewicz, P. Włodarczyk, M. Polak, A. Wojcik, W. Maziarz, A. Kolano-Burian, L. Hawalek, *Materials* 14 (2021) 726.
- [43] L. Hou, X. Fan, Q. Wang, W. Yang, B. Shen, *J. Mater. Sci. Technol.* 35 (2019) 1655–1661.
- [44] Y. Li, K. Lv, N. Shen, X. Chen, L. Chen, F. Li, X. Hui, *J. Magn. Magn. Mater.* 530 (2021) 167915.
- [45] J. Degro, P. Vojtanik, J. Filipovsky, P. Duhaj, *Mater. Sci. Eng. B* 14 (1992) 81–86.
- [46] A.R. Yavari, A.L. Moule, A. Inoue, N. Nishiyama, N. Lupu, E. Matsubara, W.J. Botta, G. Vaughan, M.D. Michiel, Å. Kvick, *Acta Mater.* 53 (2005) 1611–1619.
- [47] Q. Wang, C.T. Liu, Y. Yang, J.B. Liu, Y.D. Dong, J. Lu, *Sci. Rep.* 4 (2014) 4648.
- [48] F. Zhu, A. Hirata, P. Liu, S. Song, Y. Tian, J. Han, T. Fujita, M. Chen, *Phys. Rev. Lett.* 119 (2017) 215501.
- [49] K. Nomoto, A.V. Ceguerra, C. Gammer, B. Li, H. Bilal, A. Hohenwarter, B. Gludovatz, J. Eckert, S.P. Ringer, J.J. Kruzic, *Mater. Today* 44 (2021) 48–57.
- [50] S. Nakamichi, S. Tsurekawa, Y. Morizono, T. Watanabe, M. Nishida, A. Chiba, *J. Mater. Sci.* 40 (2005) 3191–3198.
- [51] Y. Li, Z. Wang, W. Zhang, *AIP Adv.* 8 (2018) 056115.
- [52] S.P. Mondal, K.H. Maria, S.S. Sikder, S. Choudhury, D.K. Saha, M.A. Hakim, *J. Mater. Sci. Technol.* 28 (2012) 21–26.
- [53] G. Herzer, *Acta Mater.* 61 (2013) 718–734.
- [54] C.C. Yuan, R. Liu, C.M. Pang, X.F. Zuo, B.F. Li, S.C. Song, J.Y. Hu, W.W. Zhu, B.L. Shen, *J. Alloy. Compd.* 853 (2021) 157233.
- [55] C. Yuan, Z. Lv, C. Pang, X. Li, R. Liu, C. Yang, J. Ma, H. Ke, W. Wang, B. Shen, *Sci. China Mater.* 64 (2020) 448–459.
- [56] A.I. Taub, F. Spaepen, *J. Mater. Sci.* 16 (1981) 3087–3092.
- [57] H.B. Ke, P. Zhang, B.A. Sun, P.G. Zhang, T.W. Liu, P.H. Chen, M. Wu, H.G. Huang, *J. Alloy. Compd.* 788 (2019) 391–396.
- [58] Q.P. Cao, L.J. Sun, C. Wang, Y. Fu, S.Y. Liu, S.X. Qu, X.D. Wang, D.X. Zhang, J.Z. Jiang, *Thin Solid Films* 681 (2019) 23–31.
- [59] P. Zhang, J.J. Maldonis, Z. Liu, J. Schroers, P.M. Voyles, *Nat. Commun.* 9 (2018) 1129.
- [60] J.C. Ye, J. Lu, C.T. Liu, Q. Wang, Y. Yang, *Nat. Mater.* 9 (2010) 619–623.
- [61] A. Takeuchi, A. Inoue, *Mater. Trans.* 46 (2005) 2817–2829.
- [62] C.D. Graham, T. Egami, *Ann. Rev. Mater. Sci.* 8 (1978) 423–457.
- [63] Z.B. Li, B.G. Shen, E. Niu, J.R. Sun, *Appl. Phys. Lett.* 103 (2013) 062405.
- [64] S. Taniguchi, M. Yamamoto, *Sci. Rep. Res. Inst. Tohoku Univ. A6* (1954) 330–332.